PCCP

Accepted Manuscript

This article can be cited before page numbers have been issued, to do this please use: Z. Ghobaei Namhil, C. Kemp, E. Verrelli, A. Iles, N. Pamme, A. Adawi and N. T. Kemp, *Phys. Chem. Chem. Phys.*, 2018, DOI: 10.1039/C8CP05510F.

A Label-Free Aptamer-Based Nanogap Capacitive Biosensor with Greatly Diminished Electrode Polarization Effects

Zahra Ghobaei Namhil,[a] Cordula Kemp,[b] Emanuele Verrelli,[a,c] Alex Iles,[a] Nicole Pamme,[a] Ali M. Adawi,[a,c] Neil T. Kemp[a,c,*]

[a] School of Mathematics and Physical Sciences, University of Hull, Hull, HU6 7RX, UK

[b] School of Lifesciences, University of Hull, Hull, HU6 7RX, UK

[c] George W Gray Centre for Advanced Materials, University of Hull, Hull, HU6 7RX, UK

* Author to whom correspondence should be addressed. Electronic mail: N.Kemp@hull.ac.uk

Abstract

A significant impediment to the use of impedance spectroscopy in bio-sensing is the electrode polarization effect that arises from the movement of free ions to the electrode-solution interface, forming an electrical double layer (EDL). The EDL screens the dielectric response of the bulk and its large capacitance dominates the signal response at low frequency, masking information particularly relevant for biological samples, such as molecular conformation changes and DNA hybridization. The fabrication of nanogap capacitors with electrode separation less than the EDL thickness can significantly reduce electrode polarization effects and provide enormous improvement in sensitivity due to better matching of the sensing volume with the size of the target entities. We report on the fabrication of a horizontal thin-film nanogap capacitive sensor with electrode separation of 40 nm that shows almost no electrode polarization effects when measured with water and ionic buffer solutions, thereby allowing direct quantification of their relative permittivity at low frequencies. Surface modification of the electrodes with thiol-functionalized single strand DNA aptamers transforms the device into a label-free biosensor with high sensitivity and selectivity towards the detection of a specific protein. Using this approach, we have developed a biosensor for the detection of human alpha thrombin. In addition, we also examine frequency dependent permittivity measurements on high ionic strength solutions contained within the nanogap and discuss how these support recent experimental observations of large Debye lengths. A large shift in the Debye relaxation frequency to lower frequency is also found, which is consistent with water molecules being in a rigid-like state, possibly indicating the formation of an ordered “ice-like” phase. Altogether, this work highlights the need for better understanding of fluids in confined, nanoscale geometries, from which important new applications in sensing may arise.

Introduction

Label-free electrochemical[1] and field effect transistor[2] bio-sensors have gained enormous attention in the last decade because of their low cost, portability and high potential for impact in point-of-care applications. In combination with recent advances in nanoscale engineering and surface functionalization for immobilization and detection,[3] devices have attained extraordinary levels of sensitivity with new memristor-based Si nanowire sensors recently achieving detection levels as low as 23 attomole.[4] Nowadays, a wide range of nanogap electrodes for bio-sensing applications have been investigated (see reviews[5,6]). However, the vast majority of these are resistive based sensors.[7,8,9] Capacitive based biosensors, such as those made in this study, have been investigated much less and although they have not yet achieved the levels of sensitivity of resistive based sensors, they can provide important additional knowledge (via the frequency dependence and phase information) as well as have the same advantages of small footprint, simple instrumentation, low-cost fabrication and real-time detection. Although macroscopic sized capacitive biosensors have been used for quite some time[10] their detection capabilities have been limited because of the large electrode polarization effect, which arises from the movement of free ions to the electrode-solution interface, forming an electrical double layer. The capacitance of this layer dominates the signal at low frequency, masking relaxation effects in the bulk[11] and leading to incorrect measurement of the relative permittivity as shown in Figure 1a). True quantification of the dielectric properties of the relevant part of the material or solution has therefore relied on methods of either correcting the measurement via analytical means,[12,13] which involves the fitting of various empirical functions or modelling of the electrode polarization via long-range many-body theory, or by physical compensation of the electrode double layer itself. The latter involving the use of reference electrodes or the insertion of thin electrically insulating blocking electrodes.[14,15] However, because the electrode polarization effect is heavily dependent on the surface chemistry, electrode topography, and the involvement of both short and long-range interactions of ions at the electrode/solution interface, no simple correction techniques exists and all of these approaches pose significant flaws in the correct determination of the relative permittivity.

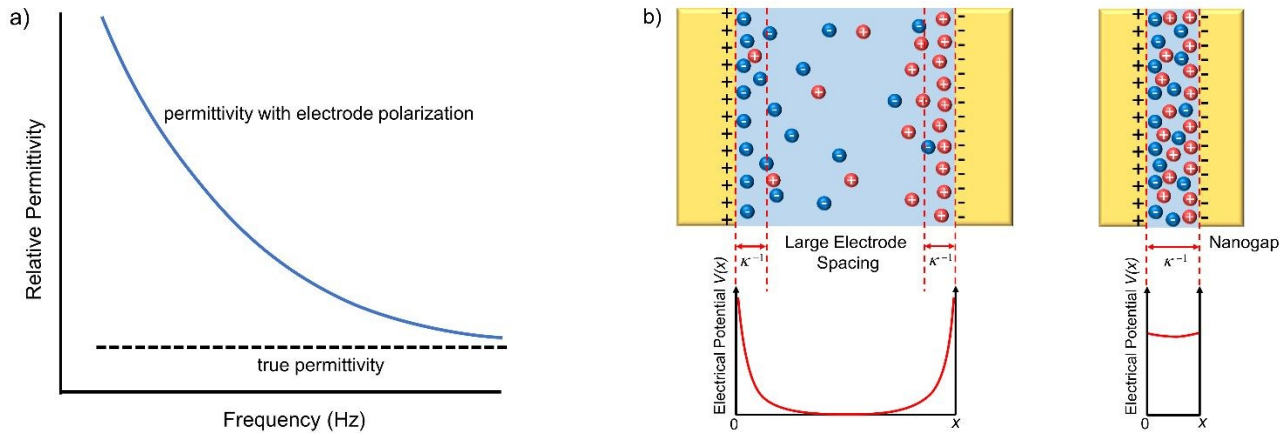

Figure 1. a) Effect of electrode polarization on measurements of the electrical relative permittivity and b) overlapping electrical double layers leads to a constant electrical potential across a nanogap device, eliminating electrode polarization effects.

Nanogap electrodes having electrode separation less than the electrical double layer (EDL) thickness, typically <100 nm, can significantly reduce electrode polarization effects since the confined region causes the electrical double layers from opposite electrodes to overlap, leading to a constant electrical potential across the nanogap region as shown in Figure 1b). This has been shown theoretically by treating the distribution of ions in the EDL in terms of the Gouy-Chapman model[16,17] and solving the Poisson-Boltzmann equation for the electrical potential. In this case, when the electrode separation, L, is less than the electrical double layer thickness, such that $L \sim 0.1\ \kappa^{-1}$ (where κ is the Debye-Hückel parameter and κ^{-1} is the Debye length) the electrical potential is almost constant across the nanogap region,[18] rather than dropping to zero in the middle of the gap. The small potential difference between the electrode interface and the middle region of the gap indicates an almost negligible contribution to the measured impedance from the electrical double layer and subsequently almost complete elimination of the electrode polarization effect. This has recently been demonstrated[19] in a vertical electrode nanogap structure whereby the relative permittivity of water at 10 Hz was measured to be $\varepsilon_r \sim 75$ in contrast to macroscopic spaced electrodes where significant electrode polarization effects instead give a value many orders of magnitude larger, $\varepsilon_r \sim 1.5\times10^6$.

Reduction of the gap size to nanoscale lengths in impedance spectroscopy also provides enormous advantages for the detection of surface bound species, since in comparison to macroscopic sized devices the size of the immobilized surface species makes up a significant proportion of the dielectric volume, thereby minimizing unwanted signal contribution from other material in the bulk. The use of short-chain single stranded nucleic acid aptamers for surface functionalization is particularly useful in this respect, since these molecules possess very high selectivity towards only the desired target species. In recent years[20,21,22] the use of aptamers in biological sensing and the early detection of diseases has rapidly increased due to increased availability of aptamer types, better understanding of surface-immobilization techniques and advances in nanotechnology that have greatly improved device sensitivity. Aptamers are single-stranded nucleic acids (RNA, DNA) that possess unique binding capabilities in contrast to more traditional recognition elements, such as antibodies and enzymes. Aptamers have much greater stability and can be used for a wide variety of target molecules, including proteins, peptides, small organic molecules, metal ions, and even large supramolecular complexes such as cells and viruses. Aptamers are also readily produced in high concentration with specific sequence structures and are easily modified with linkers and functional groups. Thus, the combination of a nanogap impedance spectroscopy with aptamer functionalized

electrodes provides a powerful but simple label-free approach for the detection of target analytes with very high specificity and selectivity. The possibility to use low frequency electrical measurements, as shown in this work, may also prove to be particularly important since it could be used to detect large-scale changes in molecular structures, such as binding events and conformation changes in DNA. We should also note that the use of electrical detection methods in contrast to optical methods, which tend to require a larger footprint due to the need of both optical sources and detectors, mitigates the potential development of small, low cost, electronic handheld sensors.

In this work we demonstrate a new, simpler and low cost approach for making a nanogap device with a planar geometry and with electrodes that are metallic. This work contrasts with two previously reported nanogap biosensor devices that have significant differences in their design, use and experimental results. The first (earlier) device had a horizontal oriented nanogap[18] but with electrodes made from silicon. This work also did not use aptamer functionalized electrodes and therefore was non-specific against the target species. The second nanogap device had a vertical oriented nanogap[19] with gold electrodes and used aptamer functionalized electrodes but had a more complicated fabrication process and a more difficult geometry for connecting the nanogap capacitors in parallel. Our results importantly discriminates between the two sets of different experimental data obtained in these earlier reports, showing the importance of using metallic electrodes rather than silicon, whilst also confirming that electrode polarization effects can indeed be greatly diminished with the use of nanogap electrodes.

To demonstrate a working prototype biosensor we have chosen human alpha thrombin as a target protein as this is a commonly used standard in the field. Thrombin is a Na^+ activated protease enzyme that is central to the formation of blood coagulants during injury. It is not present in blood under normally circumstances but is instead generated from an inactive form, prothrombin (coagulation factor II), following an injury. During the clotting process prothrombin is cleaved to form thrombin, which clots blood through the conversion of fibrinogen into fibrin. As well as many blood related illnesses involving the improper coagulation of blood the detection and monitoring of thrombin and prothrombin is important in understanding many illnesses such as Alzheimer's disease and cancer. The detection range of thrombin in blood varies widely from pM to μM depending on the injury or disease under investigation.[23]

Sensor Design

A focus of the sensor design was to improve upon the two earlier reported nanogap sensors, utilizing the advantages of both but also making the device fabrication more suited for commercialization. In contrast to the first nanogap study,[18] which utilized silicon electrodes, it was important to use a fabrication methodology that permitted the use of metallic electrodes, since this allows the use of

thiol functionalized aptamers, which would give the device both very high specificity and immobilization of the target protein directly within the active sensing region. Immobilization of the aptamer and target protein allows the device to be rinsed so as to remove unbound proteins and aptamers that affect both the specificity and sensitivity of the device. We particularly note here that aptamers were not used in the first nanogap biosensor study. Instead, the bio-sensor detected only whether DNA material was present in the sensor, meaning there was no specificity. The DNA was either measured in the solution or after evaporation of the buffer solution, the latter potentially problematic since this would leave behind ionic salts from the buffer in the process. Another potential problem of this study is that silicon and polysilicon electrodes were used that is likely to have influenced the dielectric response of both the water and ionic solutions measured as their response was not flat in the low frequency region and the relative permittivity value found for water was very different to the known theoretical value. In addition to a contribution to the overall permittivity from the native silicon oxide layer, the different value measured for water may also have resulted from strong van der Waals interactions with the underlying crystalline Si atoms, which influences ordering of molecules within the first 4 nm of the liquid layer.[24]

Our sensor design also focussed on simplification of the fabrication process so that it was more suitable to commercialization. A horizontal nanogap architecture utilizing metallic crossbar electrodes was chosen for simplicity in fabrication, since standard photolithography techniques can be used. This contrasts with the second reported nanogap study[19] in the literature, which instead used a vertical nanogap architecture. However, this involved a complicated device fabrication process that included additionally depositing a silicon nitride layer and a convoluted final lift-off procedure involving planarization of the Au electrodes by chemical-mechanical polishing. Instead, our methodology uses only a simple two-step photolithography method and a single HF etching step. Furthermore, low cost glass substrates can be used and only small quantities of gold are evaporated during the process, i.e. two 50 nm thick gold evaporation in contrast to two 1 micron thick gold evaporations.

Experimental

1. Nanofabrication

The schematic of the nanogap bio-sensor device is shown in Figure 2 and consists of top and bottom gold electrodes separated by a SiO_2 support layer. Device fabrication involved standard photolithography processes for the metal electrodes and an etching step to form the nanogap cavity. The simple techniques involved in the device fabrication are key advantages of this method and should enable low cost fabrication of devices in relatively large quantities. Figure 3 demonstrates the main sequence of steps used in the fabrication. A highly polished flat quartz substrate was first

cleaned using acetone, isopropanol and de-ionized water in an ultrasonic bath. The substrate was then coated with the adhesion promoter TI prime followed by the image reversal photoresist AZ5214E (MicroChemicals) for the first photolithography step. An image reversal photoresist was used to give inclined side-walls for improved removal of the metal layer during lift-off. Metallization of the first layer electrodes consisted of 5 nm (chromium) and 50 nm (gold), deposited using an HHV Auto 500 e-beam evaporator. Following this, a 40 nm SiO_2 dielectric layer, acting as a sacrificial/support layer, was deposited by RF magnetron sputtering deposition (at 100 W). The process gas consisted of an argon:oxygen ratio of 3:1 at $1.2x10^{-2}$ mbar with the substrate held at 300°C, to improve stoichiometry and minimize leakage current. The second photolithography step was used to form the top metal electrode. A similar method to the first photolithography step was used for this procedure. To make the nanogap, wet etching of the sacrificial SiO_2 layer was carried out using a weak solution of DI water:HF in a ratio of 10:1. Figure 4a) shows an SEM image of a typical etched nanogap with 40 nm separation between the top and bottom electrodes. The final device is shown in Figure 4b) with each device consisting of 100 capacitors in parallel. This is used to increase the overall device capacitance so that is in an acceptable range (~ pF) for ease of measurement. A protective resist, observable in the optical photo as the outer region around the square window, was also used so that only the active sensing region came into contact with the solution.

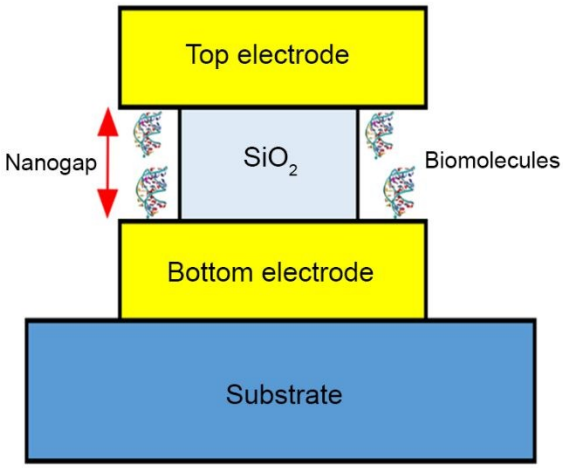

Figure 2. Schematic of the biosensor device structure consisting of top and bottom gold electrodes separated by an etched SiO_2 support layer. Binding of biomolecules to the aptamer functionalized electrodes modifies the impedance between the top and bottom electrodes.

View Article Online
DOI: 10.1039/C8CP05510F

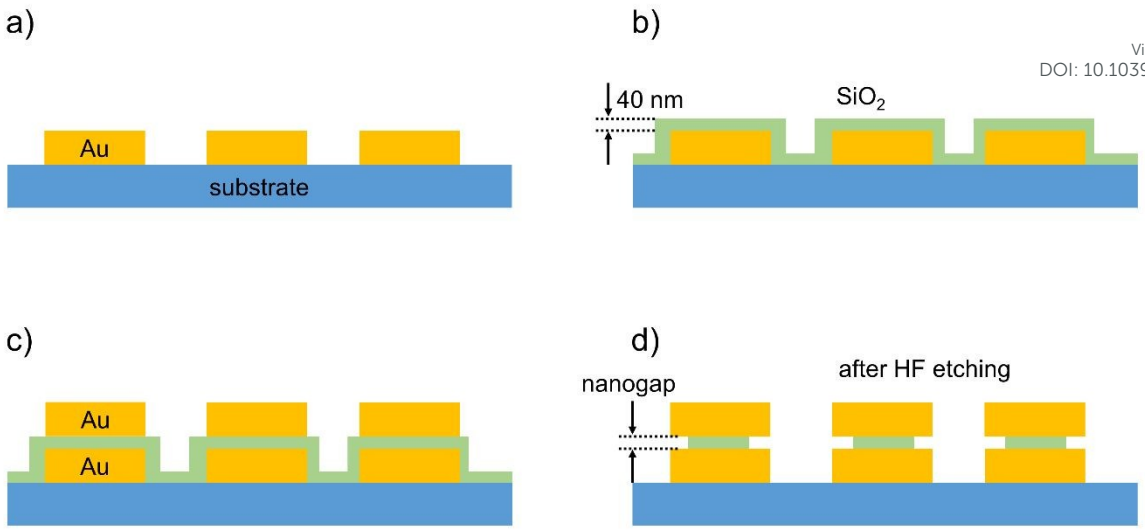

Figure 3. Fabrication steps used to construct the biosensor. a) Deposition of the bottom electrode using standard photolithography with a metallization and lift-off process, b) deposition of a 40 nm thick SiO_2 layer by RF magnetron sputtering, c) deposition of the top electrode using photolithography, and d) HF etching of the SiO_2 layer to form the nanogap space between the two electrodes.

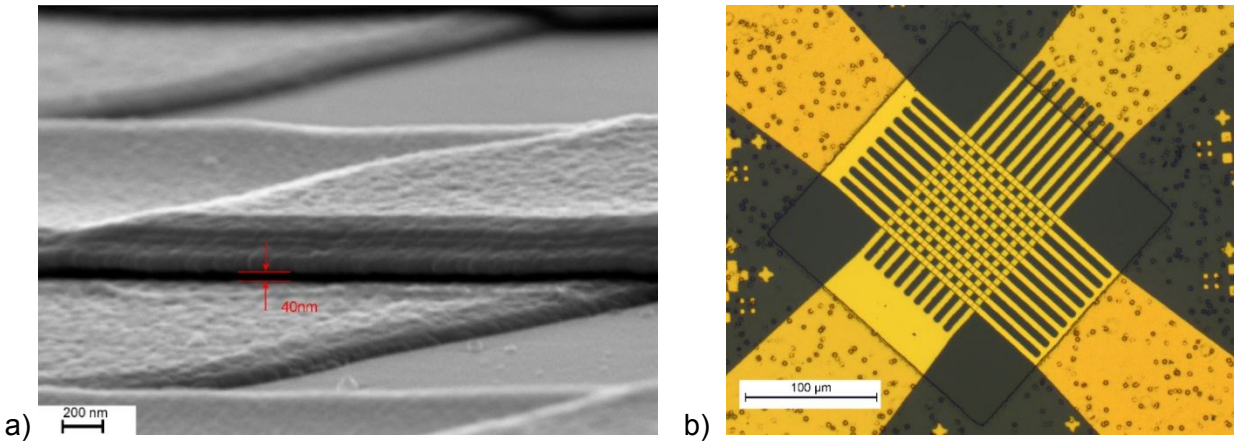

Figure 4. a) SEM image of the etched region of the nanogap biosensor confirming a 40 nm etched gap seprates the top and bottom electrodes. b) Optical image of the final nanogap sensor consisting of 10 by 10 overlapping crossbar electrodes to form 100 active capactors in parallel. The outer region of the device (dotted) is a protective resist so that only the active sensing region comes into contact with the solution.

2. Surface Functionalization

Surface functionalization by the DNA oligonucleotide was carried out using the following process. The thiol modified aptamer for thrombin with sequence[25] oligo 5'-GGT TGG TTT GGT TGG TTT/3-

$(CH_2)_3$SH-3' (Integrated DNA Technologies) was purchased in its protected S=S form. Reduction was carried out by treating the oligo (100 μM) with DTT (10 mM). The DTT was subsequently removed by passing the mixture through a Sephadex column. The aptamers were denatured at 90°C for 5 min and left to cool to room temperature to ensure correct folding. Functionalization involved a co-immobilization process with mercaptohexanol (MCH) acting as a surface blocking-agent, as well as a spacer between aptamers, providing sufficient room to enable hybridization with the target molecules.[26] The co-immobilization process involved incubating the device with 1 μM of aptamer + 100μM MCH in a PBS buffer (0.1 M, pH 7.0) overnight in the presence of a moist atmosphere to prevent the solution from evaporating. Afterwards, repeated backfilling for 50 min in a 1 mM MCH solution was used to block any remaining sites and lift any aptamers bending down on the surface.

Detection of protein binding involved first incubating the functionalized devices with the protein mixture for two hours at room temperature, followed by washing multiple times with 0.5xSSC buffer solution, in order to remove any unbound protein. The protein solution consisted of 1 μM of human α-Thrombin (HCT-0020 purchased from Cambridge BioScience) in 0.5xSSC buffer. Capacitance measurements in the presence of the buffer solution were then used to detect changes in the capacitance of the device due to the presence of the protein.

A non-binding control oligonucleotide was used to confirm if changes in the relative permittivity are due to hybridization of the thrombin with the oligonucleotide. The control oligo, having the structure 5'-GTG TGT GTG TGT GTG TTT-$(CH_2)_3$SH-3', does not have the correct nucleotide sequence for forming the G quadruplex structure that is necessary for specific binding, and therefore cannot bind to the human alpha thrombin. Experiments were carried out in exactly the same manner as above except that the control oligonucleotide was used instead to functionalize the devices.

3. AC Impedance Measurements

To characterise the devices impedance spectroscopy measurements were taken over the range of 10 Hz to 600 kHz using 0 V DC bias and a 10 mV AC signal with a Solartron 1260 impedance analyser and Solartron 1296 dielectric interface. In some cases, a Stanford SR830 Lock-in amplifier was additionally used. The devices were tested in air and de-ionized water as well as a range of dilutions of saline-sodium citrate buffer (SSC) varying from 0.1×SSC to 1.0×SSC, whereby a stock 20×SSC solution consisted of 3.0 M NaCl and 0.15 M sodium citrate buffered to pH 6.8.

View Article Online
DOI: 10.1039/C8CP05510F

Results

The impedance spectroscopy results for air, water and buffer solutions ranging from 0.1 x SSC to 1 x SSC are shown in figure 5. The relative permittivity values are determined directly from the measured capacitance results and are uncorrected for any electrode polarization effects. The relative permittivity of the solution with the gap, $\varepsilon_{calc,}$ is determined from the following equation for the measured capacitance of the sensor, $C_{meas} = 100 \times (\varepsilon_{calc}\varepsilon_0\frac{A}{D} + \varepsilon_{SiO_2}\varepsilon_0\frac{A_{SiO_2}}{D})$, where 100 is the number of capacitors in parallel, *A* is the total area of the active sensing region of a single capacitor device (2 × 5 μm × 0.8 μm), *D* is the nanogap separation (40nm) and A_{SiO_2} and ε_{SiO_2} are the area (5 μm × 3.4 μm) and relative permittivity of the SiO_2 support layer respectively. The relative permittivity calculation assumes a 0.8 micron undercut etch on either side of each SiO_2 support layer (determined by comparing the capacitance of the device before and after etching) and a relative permittivity of the SiO_2 of 3.8 (measured independently using a metal oxide semiconductor approach).

The relative permittivity (ε') results for air, deionized water and the buffer solutions are particularly interesting since they all exhibit a flat response at low frequency, indicating the absence of the electrode polarization effect. In the case of air, since there is no electrical double layer present, the relative permittivity is constant over the entire range from 10 Hz to 500 kHz. Deionized water instead shows a flat response at low frequency but undergoes a broad transition to lower relative permittivity from about 200 Hz onwards, reaching a value approaching of 1 at around 100 kHz. This result is very similar to another report of a nanogap device[19] with similar electrode spacing but is very different to the accepted value of the relative permittivity of water in macroscopic systems, which almost matches the ideal Debye relaxation model and has instead the step to lower permittivity at much high frequency, typically in the vicinity of 2-20 GHz.[27,28] The possible reasons behind these differences may be related to the confined environment of the water molecules within the nanogap and the potential formation of an ice-like phase.[18,19] The discussion section examines this possibility in more detail. The measured value of the static relative permittivity of water in the nanogap, $\varepsilon_r \approx 93$, is larger than the accepted value of water,[29] which ranges from $\varepsilon_r = 78.30$ to $\varepsilon_r = 78.58$ (at 25°C). The relative permittivity value is however very close to the measured static relative permittivity value of ice (Ih)[30,31] with a hexagonal crystalline structure, $\varepsilon_s \approx 91.5$, which lends further support to the possibility that water in the nanogap may be in a highly ordered state. This is debated further in the discussion section. We should also stress that the value measured is likely to be affected by uncertainty in the length of the undercut etch on either side of the SiO_2 support, as well as changes in surface roughness and uniformity in the nanogap thickness across the device. The presence of air bubbles in the nanogap can also not be ruled out.

Figure 5 also shows the results of the relative permittivity of different concentration SSC buffer solutions. These show many similarities to deionized water in the nanogap. The dielectric response is flat below a frequency of approximately 1000 Hz for low ionic concentration, indicating the absence of electrode polarization effects, and the transition to a lower relative permittivity occurs at a similarly low frequency and with a similar shape. The static relative permittivity of the SSC buffer is however higher than water and increases with increasing SSC concentration, rising from $\varepsilon_r \approx 167$ in the case of 0.1×SSC to $\varepsilon_r \approx 262$ for 1.0×SSC. This behaviour is unexpected since the relative permittivity should instead decrease with increasing ion concentration since the presence of strong internal electric fields between ions inhibits polarization of the water molecules. However, interestingly these results are in perfect agreement with a previous report of the relative permittivity of SSC in a nanogap device.[19] The possible reasons for this occurring is detailed in the discussion section.

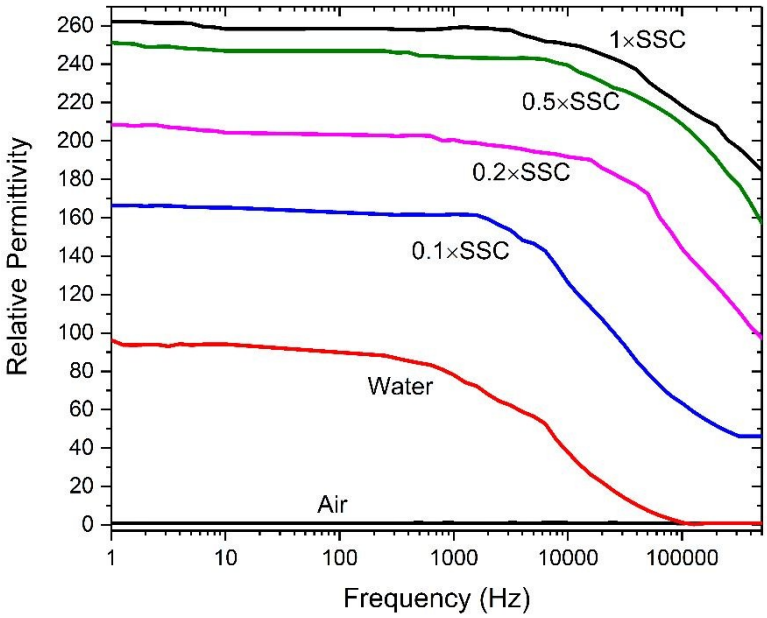

Figure 5. Relative permittivity as a function of log (frequency) for various concentrations of SSC buffer solution ranging from 0.1xSSC (blue), 0.2xSSC, (magenta) 0.5xSSC (green) and 1xSSC (black). Also shown are curves for de-ionized water (red) and air (black).

Figures 6 and 7 report on the use of the device as a biosensor. In this case, single strand nucleic acid aptamers with a sequence specific to the target protein, human α-thrombin, functionalizes the gold surfaces of the device. The device works by detecting a change in the capacitance of the device due to a change in the dielectric permittivity of the active sensing volume when the target protein molecules bind to the aptamers. The data is presented in terms of relative permittivity since capacitance is geometry specific and the contribution of the SiO_2 support structure must be taken

into consideration. The black curve in Figure 6 is the relative permittivity as a function of frequency for a bare (non-functionalized) nanogap device in the presence of the 0.5xSSC buffer solution. The same device was measured (again in a 0.5xSSC buffer) but after the aptamer functionalization process (red curve). The curve indicates an overall shift to lower relative permittivity, which is likely due to a reduction in the content of the higher permittivity buffer solution within the nanogap volume, due to the presence of the aptamers on both surface electrodes. The same device was then measured (blue curve) after a 2 hour exposure of the device to a 0.5xSSC buffer solution containing the human α-thrombin (concentration of 1 μM) and following a wash cycle with just pure 0.5xSSC buffer to remove any excess unbound proteins. The results shown in Figure 6 indicate a substantial shift to lower relative permittivity across the frequency spectrum that is consistent with binding of the lower permittivity protein within device.

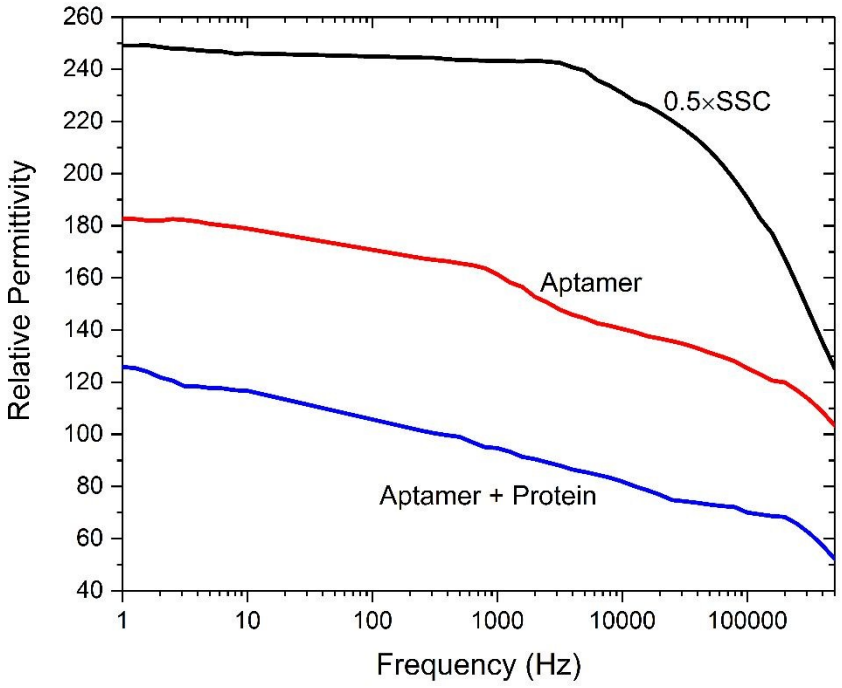

Figure 6. Relative permittivity vs log (frequency) for a bare nanogap device in the presence of a 0.5x SSC buffer (black curve), after surface functionalization with the single strand DNA aptamer (red curve), measured again in 0.5x SSC buffer, and after binding with human α-thrombin protein (concentration 1 μM in 0.5xSSC buffer solution).

Figure 7 reports measurements of the relative permittivity of devices that are instead functionalized with a non-binding control oligonucleotide. The control oligo does not have the correct amino acid sequence for forming the G quadruplex structure that is necessary for binding, and therefore cannot bind to the human alpha thrombin. Experiments were carried out in exactly the same manner as above. The black curve in Figure 7 is the relative permittivity as a function of frequency for the case

of a bare (non-functionalized) nanogap device in the presence of the 0.5xSSC buffer. The same device was measured, again in a 0.5xSSC buffer, but after the functionalization process with the control aptamer (red curve). The data demonstrates an overall shift to lower permittivity, similar to that observed in Figure 6, indicating successful surface functionalization. The same device was then measured (blue curve) after a 2 hour exposure of the device to a 0.5xSSC buffer solution containing the human α-thrombin (concentration of 1μM) and following a wash cycle with just pure 0.5xSSC buffer. In contrast to Figure 6, there is no shift to lower permittivity in this case, indicating the protein has not bound to the control aptamer. Interestingly there is a slight shift to higher permittivity in the higher frequency part of the spectrum. The cause of this is not yet fully understood but will be examined in future studies.

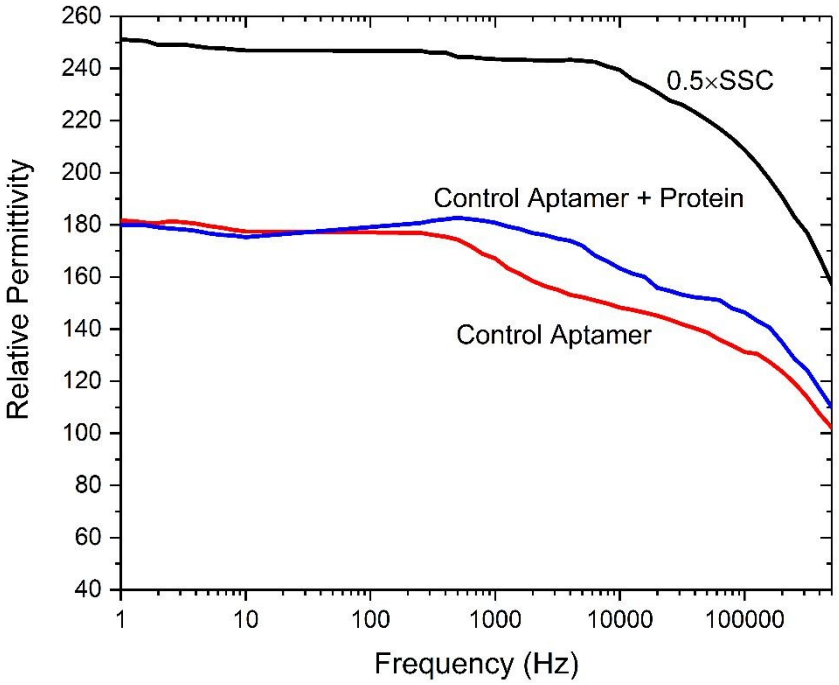

Figure 7. Relative permittivity vs log (frequency) for a bare nanogap device in the presence of a 0.5x SSC buffer (black curve), after surface functionalization with a control (non-binding) single strand DNA aptamer (red curve), and after exposure to human α-thrombin protein (concentration 1 μM in 0.5xSSC buffer solution). In this case, the immobilized control oligomer is incapable of forming the active G-quadruplex structure with the protein so hybridization should not occur.

Figure 8 gives the results of calculations of the electrical double layer thickness (EDL) of various dilutions of the 20xSSC stock solution buffer. The EDL values were determined using a self-consistent numerical approach involving the calculation of the ionic strength of the solution based on the Extended Debye Hückel model and Davies equations. The process involved determining the

concentration of the ions present in the SSC buffer (Na^+, Cl^-, OH^-, H^+) as well as those in the following reactions (using the Henderson-Hasselbach equation).

View Article Online
DOI: 10.1039/C8CP05510F

$$H_3cit \leftrightarrow H_2cit^- + H^+$$

$$H_2cit^- \leftrightarrow Hcit^{2-} + H^+$$

$$Hcit^{2-} \leftrightarrow cit^{3-} + H^+$$

$$NH_3^+ OH \leftrightarrow NH_2OH + H^+$$

The molar concentrations of the ions are used to determine the total ionic strength of the solution using:

$$I = \frac{1}{2}\sum_i z_i^2 c_i \quad (1)$$

where I = total ionic strength of the solution and c_i and z_i are the molar concentration and charge of ion i. However, since the activity coefficients and equilibria constants are dependent upon the ionic strength, the molar concentrations of the ions must be re-calculated iteratively until convergence is reached.

The EDL thickness (κ^{-1}), or Debye length (or Debye-Huckel parameter), can then be determined using:

$$\kappa^{-1} = \sqrt{\frac{\varepsilon_r \varepsilon_0 k_B T}{2 N_A e^2 I}} \quad (2)$$

where ε_r is the dielectric constant (or relative permittivity), ε_0 is the permittivity of free space, k_B is the Boltzmann constant, T is the temperature, N_A is the Avogadro number, e is the elementary charge and I is the ionic strength (note: mol/m^3). In the case of water (ε_r=78) at 25°C this can be simplified to:

$$\kappa^{-1}(\text{nm}) = \frac{0.304}{\sqrt{I}} \quad (3)$$

where κ^{-1} is expressed in nanometer and I is in mol/L.

The graph shown in Figure 8 depicts the typical decay of the EDL thickness with increasing ionic strength and indicates that at low 0.001xSSC concentrations the EDL layers overlap since the EDL thickness on just one of the electrodes is ≈ 20 nm, whilst in the case of buffer solutions used in typical impedance spectroscopy measurements (and in this work i.e. 0.5xSSC concentration), the EDL is very small, ≈ 1 nm, and would importantly, appear to not overlap. Implications of this in relation to the effectiveness of the device and dielectric response, which surprisingly still appears flat at low frequency, are detailed in the discussion section.

View Article Online
DOI: 10.1039/C8CP05510F

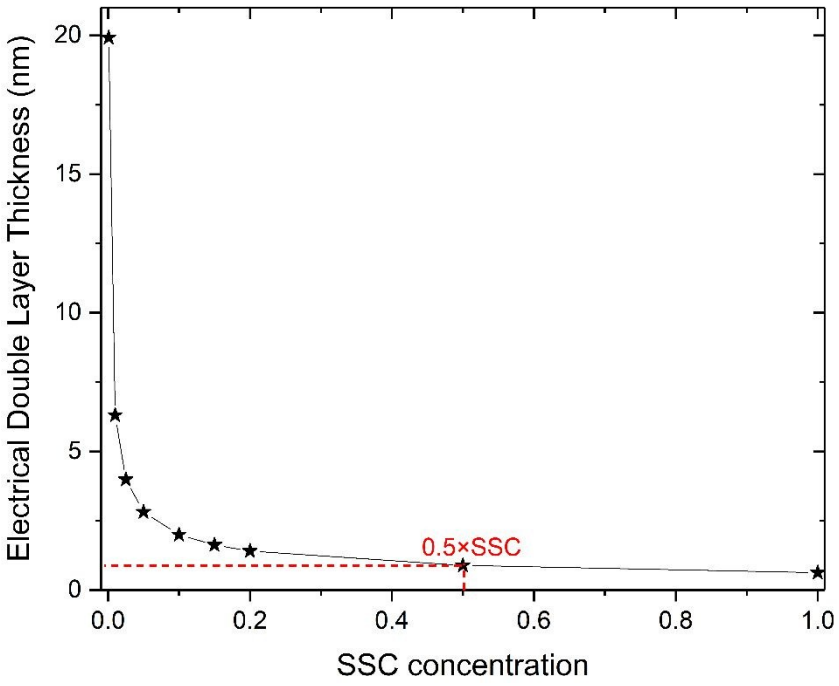

Figure 8. Electrical double layer thickness vs concentration of the SSC buffer determined from numerical calculations based on the Extended Debye Hückel model and Davies equation.

Discussion

1. Nanogap Bio-sensing

Our results demonstrate successful operation of the device as a biosensor for the detection of small proteins with high specificity and sensitivity. Figure 6 shows that binding of human α-Thrombin to the aptamer functionalized surface leads to a 32% decrease in the measured relative permittivity at 1 Hz. In contrast, when a non-binding control aptamer was used, there was no decrease in the relative permittivity. Importantly, the figure indicates the device is most sensitive at low frequencies, which can be attributed to almost complete elimination of electrode polarization effects, which would otherwise normally swamp the device response and masking all important information in this frequency range. Low frequency detection measurement are particularly important since it can be used to better detect large-scale changes in molecules structures, such as binding events and conformation changes of DNA. In this study the reduction in the relative permittivity after binding of the protein is largely attributed to replacement of the high relative permittivity solution (0.5xSSC) in the nanogap region with the low relative permittivity protein. However, as discussed further below, the nature of the dielectric response of both water and high ionic strength solutions when contained in nanogaps is poorly understood, and this is made particularly more complex due to the presence of the aptamer and protein molecules at the electrode surfaces, whose additional effect on the electrical double layer and possible ordering of the solution molecules is unknown.

In this article, we have not investigated the detection limits and sensitivity of the device, which will be reported in future work. From a theoretical perspective, we expect the ultimate detection limit is in the vicinity of the attomolar range. This is based on a total sensor area of 1600 μm^2 (active area of the 100 capacitors including top and bottom electrodes) with coating of the aptamer molecules[32] at approximately 10^4 mol/μm^2 to give the number of aptamer probes per device as 16×10^6 mol. For the situation in which all of the aptamer probes have bound protein molecules the device sensitivity would be 16×10^6 mol / $6.022\times10^{23} = 30\times10^{-18}$ mol.

The nanogap biosensors, once fabricated, have good repeatability (80 - 90 %) between different devices and also with repeated measurements. A greater challenge is the yield of successful devices during fabrication. Currently this is only about 15 %. A number of improvements can be made to greatly increase the yield of working devices, such as improving the adhesion of the electrodes to the underlying substrate and increasing the robustness of the top electrode. Optimization of these will allow more rigorous studies of the upper limit of the device sensitivity and investigations of different aptamer/protein types as well as their use in biological relevant fluids. These will be examined in future work.

2. Nature of the Dielectric Response and Electrical Double Layer in Nanogap Devices

The nanogap capacitor device shows almost complete absence of electrode polarization, which indicates very good applicability of the device in bio-sensing. However, the permittivity results raise a number of interesting issues concerning the nature of the electrical double layer and the dielectric relaxation mechanisms of water and ionic solutions when confined in nanoscale dimensions.

The first issue concerns the nature of the dielectric response in the case of when only de-ionized water is present within the nanogap. The real permittivity shows a flat response at low frequency but undergoes a broad transition to low values from about 200 Hz onwards, reaching a value approaching 1 at around 100 kHz. This is very different to the accepted relative permittivity values of water in macroscopic systems, which almost match the ideal Debye relaxation model and have instead a step to lower relative permittivity at much high frequency, typically in the vicinity of 2-20 GHz.[27,28] The occurrence of the step at much lower frequency is possibly because of the inability of the water molecules' dipole moment to sufficiently polarize in synchronization with the alternating electric field. It has been previously suggested[18,19] that water in the nanogap may be in an ice-like phase, and indeed the dielectric response has many similarities with relative permittivity values of ice, which has almost the same real and imaginary permittivity features of liquid water,[33] but are shifted to lower frequency by 10^6 Hz. Ice has as many as 17 known crystalline forms, each having different frequency dependent permittivity.[34,35,36,37] A comparison of our data with frequency dependent relative permittivity measurements on pure ice[38] over a range of temperature, -57°C to -0.1°C, indicates that our data, although having a slightly broader transition ranging from 200 Hz to

100 kHz, is most similar to that of ice at a temperature of -20°C to -0.1°C. The most common phase transition is hexagonal crystalline ice (phase Ih), which occurs when liquid water is cooled to 0°C at standard atmospheric pressure. The frequency response of the relative permittivity of ice Ih at 0°C and it's static relative permittivity,[30,31] $\varepsilon_s \approx 91.5$, are both in agreement[33] with that of water in the nanogap device.

The question of whether water molecules can truly retain an ice-like structure over distances greater than a few atomic length scales is however still a topic of debate. Recent new experiments have given much insight to the adsorption of water monolayers on metals and the structure of the first few molecular layers. The work has challenged the commonly held theory of a bi-layer structure,[39] consisting of a buckled hexagonal overlayer resembling the basal plane of ice. However, beyond the first few layers, and especially at ambient temperatures, there is still limited understanding on the structure and dynamics of both multilayer water adsorption and liquid-water thin-films on surfaces.

In the case of the nanogap device the presence of strong electric fields within the electrical double layer must also be considered as these can easily reach up to 10^8 -10^9 V/m in the Helmholtz layer directly adjacent to the electrode. Electric fields orient the water molecules depending on its direction; a positively charged electrode orients water so that its hydrogen atoms are directed away from the surface whilst a negatively charge electrode orients the hydrogens to be instead directed toward the surface. Molecular dynamics simulations of water lamina embedded between two platinum electrodes[40] have shown that without the presence of an electric field, the first adsorbed layer has a solid-like state whilst the second and third layers are liquid but with an orientation distribution favouring a hexagonal ice formation. However, with an electric field of 2×10^{10} V/m present, simulations have shown the water molecules reorient, aligning their dipoles along the field. A large change in the density profile is predicted and the water undergoes crystallisation process to give a cubic ice structure (phase I_C). A similar point of view was also found in another study that examined the dielectric response,[41] where it was shown the polarization underwent a non-linear transition starting from $\approx 0.1\times10^9$ V/m, whilst at higher electric fields, above 30×10^9 V/m, a phase transition occurred to a completely ordered ice-like structure. Experimental verification of results in this area is challenging however, and it is likely that other effects are also important, since impurities, defects and surface roughness may stimulate or inhibit crystallization and high electric fields are known to modify electrochemical reaction rates as well as promote the ionization[42] of water. In this context, the nanogap devices could prove to be a useful probe to better understand such effects and improve the understanding of how molecules order and interact at liquid-metal interfaces.

The second issue concerns the increase in the relative permittivity of the SSC buffer with increasing concentration. The higher relative permittivity indicates greater polarizability of the solution with increasing SSC concentration, which contrasts with that of macroscopic measurements on ionic solutions whereby the relative permittivity instead reduces with increasing salt concentration due to the effect of the electric field of the ions inhibiting the external electric field.[43] For example, the accepted model in the case of a simple ionic solution, such as NaCl, is that the polar water molecules align themselves with the electric fields of the dissociated sodium and chloride ions, forming a hydration shell around individual ions. The water molecules are then less able to respond to the external electric field, which has the effect of lowering the dielectric constant. In a dilute solution with (<1.5 M) the relative permittivity decreases linearly with salt concentration with the relationship[44] $\varepsilon_r = \varepsilon_w - \alpha c$, where c is the salt concentration, α is an ion specific constant and ε_w is the dielectric constant of pure water. The absence of this relationship in our data, which also supports results from other studies,[18,19] is intriguing and requires further work to understand its cause.

The third area requiring further understanding is whether the electrical double layer (EDL) is really overlapping in the case of when the biosensor is used with the relatively high concentration SSC buffers. In the case of pure water it is straightforward to show the electrical double layers overlap. For weak ionic strength solutions, the Debye-Hückel regime is appropriate and the Debye screening (equation 2) is the governing length scale, giving a value of $\kappa^{-1} \approx 1$ μm for pure water at 25°C, indicating a large overlap of the electrical double layers. However, the Debye-Huckel theory is only valid in this dilute regime, where the total ionic strength is I <0.005 M. At higher concentration, either the extended Debye-Hückel (I <0.1 M) or the Davies equation (I <0.5 M) should be used. The graph in Figure 8 give the results of calculations of the EDL thickness of various dilutions of the 20xSSC stock solution buffer. From this, it is transparent that the EDL thickness of the 0.5xSSC buffer solution has a relatively short electrical double layer thickness (≈ 1 nm), which is much less than the 40 nm gap separation of the electrodes. Thus, it is not clear in this model if the EDL's are indeed overlapping. However, interestingly the electrode polarization effects still appear to be negligible because of the flat response in the frequency dependent permittivity.

Recent investigations[45] involving the measurement of the screening length between two planar charged mica surfaces containing high ionic solutions indicates may shed some light on this dilemma. In contrast to classical electrolyte theories of dilute electrolytes, which indicates diminished screening at higher ionic concentrations, the measurements reported instead showed an increase in screening length with electrolyte concentration. This study has created much excitement in the field and a plethora of reports of long range screening lengths on a wide range of ionic liquids and salt solutions,[46,47,48,49] as well as attempts to explain these puzzling observations.[50,51,52,53] Although the

theory is not well understood, it is apparent from these recent studies that long range double layers can possibly be present in such systems with lengths of 10 nm or more. This effect could help to explain why increasing permittivity values were found with increasing ionic strength, and the lack of correlation between the large observed changes in the measured static relative permittivity (Figure 5) and the relatively small change in the EDL length for concentrations between 0.2×SSC and 1.0×SSC (Figure 8).

Lastly, we would like to emphasize the need for further work in the area so that a better understanding can be gained of one of the most important, yet unique and puzzling materials on this planet.[54] Water plays a central role in life, biology, science and technology. It dominates a variety of solvation and charge transfer phenomena. However, because of its peculiar properties imbibed from its molecular structure, which enables a strong dipole moment and weak van der Waals interaction, many of its properties are still not fully understood. The understanding of water in confined regions is hugely important for numerous fields, including biological systems (e.g. the interaction of proteins in cells), materials science (e.g. clays), chemistry (e.g. colloids) and the development of new technologies (e.g. electrolytic batteries and hydrogen fuel cells). Further studies on the origin of the dielectric relaxation in nanogap systems may help better understanding of the long running debate on the molecular origins of the Debye relaxation in water, which is a topic that is still under considerable debate.[55]

Conclusions

We report on a horizontal thin-film nanogap capacitive sensor with electrode separation of 40 nm, fabricated using only standard photolithography techniques. The confined geometry of the active sensing region of the device causes overlap of the two electrical double layers when a low ionic strength solution is present within the 40 nm separated electrodes. Frequency dependent dielectric spectroscopy results indicates no electrode polarization effects are present when measured with either water or ionic buffer solutions, which greatly enhances the application of the devices since it enables low frequency measurements to be used for detection. By functionalizing the device electrodes with thiol-immobilized single strand DNA aptamers we have successfully fabricated a working nanogap biosensor targeted for the detection of human alpha thrombin. The wide range of aptamers variants available along with the simplicity of the device fabrication should enable use of the biosensor for the early detection of many diseases types. We as well discuss the interesting dielectric response of water and high ionic strength solutions contained within the nanogap device.

Conflicts of Interest

There are no conflicts of interest to declare.

View Article Online
DOI: 10.1039/C8CP05510F

Acknowledgements

We gratefully acknowledge the University of Hull PhD Scholarship scheme for funding of this research as well as the work of Tony Sinclair in carrying out the SEM investigations and help from Dr Chris Walton in microscopy work and thin-film investigations.

References

1 P. Jolly, V. Tamboli, R. L. Harniman, P. Estrela, C. J. Allender and J. L. Bowen, Aptamer-MIP hybrid receptor for highly sensitive electrochemical detection of prostate specific antigen, *Biosens. Bioelectron.*, 2016, **75**, 188–195.

2 A. Poghossian and M. J. Schöning, Label-Free Sensing of Biomolecules with Field-Effect Devices for Clinical Applications, *Electroanalysis*, 2014, **26**, 1197–1213.

3 E. Stern, J. F. Klemic, D. A. Routenberg, P. N. Wyrembak, D. B. Turner-Evans, A. D. Hamilton, D. A. LaVan, T. M. Fahmy and M. A. Reed, Label-free immunodetection with CMOS-compatible semiconducting nanowires, *Nature*, 2007, **445**, 519–522.

4 I. Tzouvadaki, P. Jolly, X. Lu, S. Ingebrandt, G. De Micheli, P. Estrela and S. Carrara, Label-free ultrasensitive memristive aptasensor, *Nano Lett.*, 2016, **16**, 4472–4476.

5 T. Li, W. Hu and D. Zhu, Nanogap Electrodes, *Adv. Mater.*, 2010, **22**, 286–300.

6 X. Chen, Z. Guo, G. Yang, J. Li, M. Li, J. Liu and X. Huang, Electrical nanogap devices for biosensing, *Mater. Today*, 2010, **13**, 28–41.

7 S. K. Kim, H. Cho, H. Park, D. Kwon, J. M. Lee and B. H. Chung, Nanogap biosensors for electrical and label-free detection of biomolecular interactions, *Nanotechnology*, 2009, **20**, 455502.

8 H. Zhang, W. Xu, X. Liu, F. Stellacci and J. T. L. Thong, Capturing a DNA duplex under near-physiological conditions, *Appl. Phys. Lett.*, 2010, **97**, 163702.

9 M. Tsutsui, M. Taniguchi, K. Yokota and T. Kawai, Identifying single nucleotides by tunnelling current, *Nat. Nanotechnol.*, 2010, **5**, 286–290.

10 J. S. Daniels and N. Pourmand, Label-Free Impedance Biosensors: Opportunities and Challenges, *Electroanalysis*, 2007, **19**, 1239–1257.

11 P. Ben Ishai, M. S. Talary, A. Caduff, E. Levy and Y. Feldman, Electrode polarization in dielectric measurements: a review, *Meas. Sci. Technol.*, 2013, **24**, 102001.

12 H. P. Schwan, Linear and nonlinear electrode polarization and biological materials, *Ann. Biomed. Eng.*, 1992, **20**, 269–288.

13 A. A. Kornyshev, Double-layer in ionic liquids: Paradigm change?, *J. Phys. Chem. B*, 2007, **111**, 5545–5557.

14 F. Pizzitutti and F. Bruni, Electrode and interfacial polarization in broadband dielectric spectroscopy measurements, *Rev. Sci. Instrum.*, 2001, **72**, 2502–2504.

15 H. Jansson, R. Bergman and J. Swenson, Hidden slow dynamics in water, *Phys. Rev. Lett.*, 2010, **104**, 017802.

16 G. Gouy, Sur la constitution de la charge électrique à la surface d'un electrolyte, *J. Phys. Radium*, 1910, **9**, 457–468.

17 D. L. Chapman, A contribution to the theory of electrocapillarity, *Philos. Mag.*, 1913, **25**, 475–481.

18 M. Yi, K. H. Jeong and L. P. Lee, Theoretical and experimental study towards a nanogap dielectric biosensor, *Biosens. Bioelectron.*, 2005, **20**, 1320–1326.

19 M. S. Mannoor, T. James, D. V. Ivanov, L. Beadling and W. Braunlin, Nanogap dielectric spectroscopy for aptamer-based protein detection, *Biophys. J.*, 2010, **98**, 724–732.

20 G. Marrazza, Aptamer Sensors, *Biosensors*, 2017, **7**, 5–7.

21 S. Song, L. Wang, J. Li, C. Fan and J. Zhao, Aptamer-based biosensors, *TrAC - Trends Anal. Chem.*, 2008, **27**, 108–117.

22 E. J. Cho, J.-W. Lee and A. D. Ellington, Applications of Aptamers as Sensors, *Annu. Rev. Anal. Chem.*, 2009, **2**, 241–264.

23 B. Deng, Y. Lin, C. Wang, F. Li, Z. Wang, H. Zhang, X. Li and X. C. Le, Analytica Chimica Acta Aptamer binding assays for proteins : The thrombin example — A review, *Anal. Chim. Acta*, 2014, **837**, 1–15.

24 D. Täuber, I. Trenkmann and C. von Borczyskowski, Influence of van der Waals Interactions on Morphology and Dynamics in Ultrathin Liquid Films at Silicon Oxide Interfaces, *Langmuir*, 2013, **29**, 3583–2593.

25 K. Y. Wang, S. Mccurdy, R. G. Shea, S. Swaminathan and P. H. Bolton, A DNA Aptamer Which Binds to and Inhibits Thrombin Exhibits Structural Motif for DNA, *Biochemistry*, 1993, **32**, 1899–1904.

26 N. Aliakbarinodehi, P. Jolly, N. Bhalla, A. Miodek, G. De Micheli, P. Estrela and S. Carrara, Aptamer-based Field-Effect Biosensor for Tenofovir Detection, *Sci. Rep.*, 2017, **7**, 44409.

27 U. Kaatze, Complex Permittivity of Water as a Function of Frequency and Temperature, *J. Chem. Eng. Data*, 1989, **34**, 371–374.

28 T. Sato and R. Buchner, Dielectric relaxation processes in ethanol/water mixtures, *J. Phys. Chem. A*, 2004, **108**, 5007–5015.

29 D. P. Fernández, Y. Mulev, A. R. H. Goodwin and J. M. H. L. S. Sengers, A Database for the Static Dielectric Constant of Water and Steam, *J. Phys. Chem. Ref. Data*, 1995, **24**, 33–70.

30 R. P. Auty and R. H. Cole, Dielectric Properties of Ice and Solid D2O, *J. Chem. Phys.*, 1952, **20**, 1309.

31 G. P. Johari and E. Whalley, The dielectric properties of ice Ih in the range 272–133 K, *J. Chem. Phys.*, 1981, **75**, 1333–1340.

32 S. L. Beaucage, Strategies in the preparation of DNA oligonucleotide arrays for diagnostic applications, *Curr. Med. Chem.*, 2001, **8**, 1213–1244.

33 V. G. Artemov and A. A. Volkov, Water and ice dielectric spectra scaling at 0°C, *Ferroelectrics*, 2014, **466**, 158–165.

34 E. Whalley, J. B. R. Heath and D. W. Davidson, Ice IX: An Antiferroelectric Phase Related to Ice III, *J. Chem. Phys.*, 1968, **48**, 2362–2370.

35 G. P. Johari and E. Whalley, The dielectric relaxation time of ice V, its partial anti-ferroelectric ordering and the role of Bjerrum defects, *J. Chem. Phys.*, 2001, **115**, 3274–3280.

36 G. P. Johari and E. Whalley, Dielectric properties of ice VI at low temperatures, *J. Chem. Phys.*, 1976, **64**, 4484.

37 G. P. Johari, A. Lavergne and E. Whalley, Dielectric properties of ice VII and VIII and the phase boundary between ice VI and VII, *J. Chem. Phys.*, 1974, **61**, 4292–4300.

38 A. D. Watt and E. L. Maxwell, Measured electrical properties of snow and glacial ice, *J. Res. Natl. Bur. Stand. (1934).*, 1960, **64D**, 357–363.

39 J. Carrasco, A. Hodgson and A. Michaelides, A molecular perspective of water at metal interfaces, *Nat. Mater.*, 2012, **11**, 667–674.

40 X. Xia, L. Perera, U. Essmann and M. L. Berkowitz, The structure of water at platinum/water interfaces Molecular dynamics computer simulations, *Surf. Sci.*, 1995, **335**, 401–415.

41 G. Sutmann, Structure formation and dynamics of water in strong external electric fields, *J. Electroanal. Chem.*, 1998, **450**, 289–302.

42 E. M. Stuve, Ionization of water in interfacial electric fields: An electrochemical view, *Chem. Phys. Lett.*, 2012, **519**–**520**, 1–17.

43 N. Gavish and K. Promislow, Dependence of the dielectric constant of electrolyte solutions on ionic concentration: A microfield approach, *Phys. Rev. E*, , DOI:10.1103/PhysRevE.94.012611.

44 J. B. Hasted, D. M. Ritson and C. H. Collie, Dielectric Properties of Aqueous Ionic Solutions. Parts I and II, *J. Chem. Phys.*, 1948, **16**, 1–21.

45 M. A. Gebbie, M. Valtiner, X. Banquy, E. T. Fox, W. A. Henderson and J. N. Israelachvili, Ionic liquids behave as dilute electrolyte solutions, *Proc. Natl. Acad. Sci.*, 2013, **110**, 9674–9679.

46 A. M. Smith, A. A. Lee and S. Perkin, The Electrostatic Screening Length in Concentrated Electrolytes Increases with Concentration, *J. Phys. Chem. Lett.*, 2016, **7**, 2157–2163.

47 M. A. Gebbie, H. A. Dobbs, M. Valtiner and J. N. Israelachvili, Long-range electrostatic screening in ionic liquids, *Proc. Natl. Acad. Sci.*, 2015, **112**, 7432–7437.

48 H. W. Cheng, P. Stock, B. Moeremans, T. Baimpos, X. Banquy, F. U. Renner and M. Valtiner, Characterizing the Influence of Water on Charging and Layering at Electrified Ionic-Liquid/Solid Interfaces, *Adv. Mater. Interfaces*, 2015, **2**, 1–9.

49 R. M. Espinosa-Marzal, A. Arcifa, A. Rossi and N. D. Spencer, Microslips to 'avalanches' in confined, molecular layers of ionic liquids, *J. Phys. Chem. Lett.*, 2014, **5**, 179–184.

50 A. Yochelis, Transition from non-monotonic to monotonic electrical diffuse layers: impact of confinement on ionic liquids, *Phys. Chem. Chem. Phys.*, 2014, **16**, 2836.

51 R. Kjellander, Decay behavior of screened electrostatic surface forces in ionic liquids: the vital role of non-local electrostatics, *Phys. Chem. Chem. Phys.*, 2016, **18**, 18985–19000.

52 Z. A. H. Goodwin and A. A. Kornyshev, Underscreening, overscreening and double-layer capacitance, *Electrochem. commun.*, 2017, **82**, 129–133.

53 M. A. Gebbie, A. M. Smith, H. A. Dobbs, A. A. Lee, G. G. Warr, X. Banquy, M. Valtiner, M. W. Rutland, J. N. Israelachvili, S. Perkin and R. Atkin, Long range electrostatic forces in ionic liquids, *Chem. Commun.*, 2017, **53**, 1214–1224.

54 H. E. Stanley, Unsolved mysteries of water in its liquid and glassy phases, *Mater. Res. Bull.*, 1999, **24**, 22–30.

55 D. C. Elton, The origin of the Debye relaxation in liquid water and fitting the high frequency excess response, *Phys. Chem. Chem. Phys.*, 2017, **19**, 18739–18749.

View Article Online
DOI: 10.1039/C8CP05510F

View Article Online
DOI: 10.1039/C8CP05510F

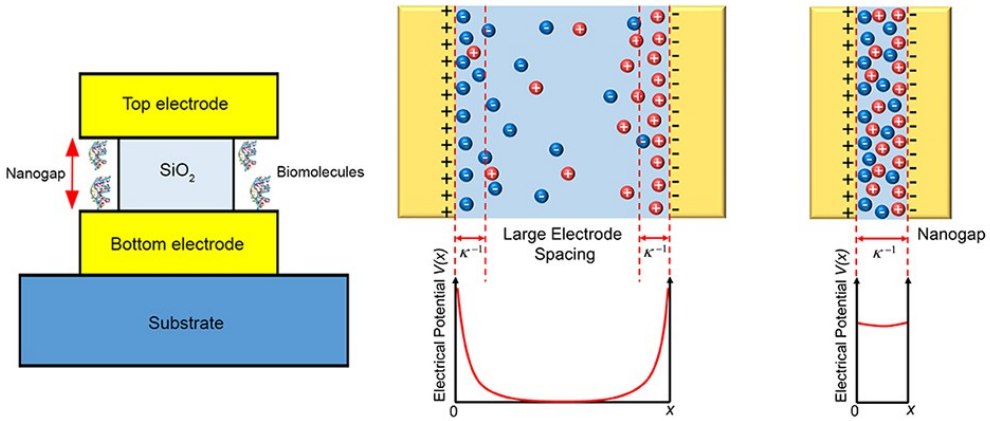

80x39mm (300 x 300 DPI)